CHEMISTRY
A EUROPEAN JOURNAL

DOI: 10.1002/chem.200601761

Electronic Perturbation in a Molecular Nanowire of $[IrCl_5(NO)]^-$ Units

Florencia Di Salvo,[a] Natalia Escola,[a] Damián A. Scherlis,*[a] Darío A. Estrin,[a] Carlos Bondía,[b] Daniel Murgida,[b] José M. Ramallo-López,[c] Félix G. Requejo,[c] Linda Shimon,[d] and Fabio Doctorovich*[a]

Abstract: The nitrosyl in $[IrCl_5(NO)]^-$ is probably the most electrophilic known to date. This fact is reflected by its extremely high IR frequency in the solid state, electrochemical behavior, and remarkable reactivity in solution. $PPh_4[IrCl_5(NO)]$ forms a crystal in which the $[IrCl_5(NO)]^-$ anions are in a curious wire-like linear arrangement, in which the distance between the N–O moiety of one anion and the *trans* chloride of the upper one nearby is only 2.8 Å. For the same complex $[IrCl_5(NO)]^-$ but with a different counterion, $Na[IrCl_5(NO)]$, the anions are stacked one over the other in a side-by-side arrangement. In this case the electronic distribution can be depicted as the closed-shell electronic structure Ir^{III}–NO^+, as expected for any d^6 third-row transition metal complex. However, in $PPh_4[IrCl_5(NO)]$ an unprecedented electronic perturbation takes place, probably due to $NO^{\bullet}$–Cl^- acceptor–donor interactions among a large number of $[IrCl_5(NO)]^-$ units, favoring a different electronic distribution, namely the open-shell electronic structure Ir^{IV}–$NO^{\bullet}$. This conclusion is based on XANES experimental evidence, which demonstrates that the formal oxidation state for iridium in $PPh_4[IrCl_5(NO)]$ is +4, as compared with +3 in $K[IrCl_5(NO)]$. In agreement, solid-state DFT calculations show that the ground state for $[IrCl_5(NO)]^-$ in the PPh_4^+ salt comprises an open-shell singlet with an electronic structure which encompasses half of the spin density mainly localized on a metal-centered orbital, and the other half on an NO-based orbital. The electronic perturbation could be seen as an electron promotion from a metal–chloride to a metal–NO orbital, due to the small HOMO–LUMO gap in $PPh_4[IrCl_5(NO)]$. This is probably induced by electrostatic interactions acting as a result of the closeness and wire-like spatial arrangement of the Ir metal centers, imposed by lattice forces due to π–π stacking interactions among the phenyl rings in PPh_4^+. Experimental and theoretical data indicate that in $PPh_4[IrCl_5(NO)]$ the Ir–N–O moiety is partially bent and tilted.

Keywords: electron transfer · iridium · nanostructures · nitrosyl · valence isomerization

Introduction

Metal nitrosyls have attracted considerable attention since the discovery of endogenous NO as a biomolecule.[1] The nitrosyl in $K[IrCl_5(NO)]$ is probably the most electrophilic electron-poor nitrosyl ("NO^+") known to date. This fact is reflected by its extremely high IR frequency in the solid state (2006 cm^{-1}),[2] electrochemical behavior,[3,4] and re-

[a] F. Di Salvo, Dr. N. Escola, Dr. D. A. Scherlis, Prof. D. A. Estrin, Prof. F. Doctorovich
Departamento de Química Inorgánica
Analítica y Química Física/INQUIMAE-CONICET
Facultad de Ciencias Exactas y Naturales
Universidad de Buenos Aires
Ciudad Universitaria, Pabellón II, piso 3
C1428EHA Buenos Aires (Argentina)
Fax: (+5411) 457-63-341
E-mail: damian@qi.fcen.uba.ar
doctorovich@qi.fcen.uba.ar

[b] Dr. C. Bondía, Dr. D. Murgida
Max Volmer Laboratory of Biophysical Chemistry
Institute of Chemistry Technical University of Berlin
Strasse des 17. Juni 135, 10623 Berlin (Germany)

[c] Dr. J. M. Ramallo-López, Dr. F. G. Requejo
INIFTA–IFLP (CONICET) and Departamento de Física
Facultad de Ciencias Exactas
Universidad Nacional de La Plata, 1900 La Plata (Argentina)

[d] Dr. L. Shimon
Department of Chemical Services The Weizmann Institute of Science, Rehovot 76100 (Israel)

Supporting information for this article is available on the WWW under http://www.chemeurj.org/ or from the author.

markable reactivity[5,6] observed in solution. According to the formalism of Enemark and Feltham,[7] the crystal structure of this hexacoordinated $\{MNO\}^6$ comprises an octahedral anion with a practically linear Ir–NO moiety (Ir-N-O 174.3°).[8]

Third-row transition metal complexes with an even number of electrons generally have a low-spin electronic distribution in the ground state, where each electron pair occupies just one orbital. This is mainly because of the considerable energy gap between the HOMO and the LUMO and the relatively low electronic repulsion. Spin crossover, a temperature-dependent low-spin to high-spin transition, is well known for first-row transition metals, especially iron,[9] but very rare for second- or third-row transition metals.

Intramolecular electron transfer involving a metal ion and a redox-active ligand can give two different electronic isomers (more specifically, valence tautomers).[10] It can be induced not only by temperature variations but also by irradiation or pressure, or other changes in the environment such as counterion changes.[11] This interconversion and the spin crossover mentioned above can be considered as entropy-driven processes. Most of the reported examples which exhibit valence tautomerism are based on quinone or quinone-type ligands with a series of transition metal ions such as Co, Cu, Ni, and Mn, and more recently Fe. No examples showing electronic transfer or promotion involving either a third-row metal such as iridium or an NO ligand have been reported yet.

Based on solid-state and in-vacuo DFT calculations, XANES, FTIR, and Raman experimental evidence, two different electronic distributions can be observed for the same anion, $[IrCl_5(NO)]^-$: Ir^{III}–NO^+ for Na^+ and K^+ salts; and Ir^{IV}–$NO^\bullet$ for PPh_4^+ and $AsPh_4^+$ ones.[12] In the second case, π–π stacking interactions among the phenyl rings could be the motive forces producing an electronic promotion from a metal-based orbital to an NO-based orbital due to a decrease in the HOMO–LUMO gap in the solid.

Results and Discussion

As expected, the crystal structure of $Na[IrCl_5(NO)]$ obtained by our group (Figure 1 and Supporting Information) is almost coincident with the structure of $K[IrCl_5(NO)]$ mentioned above and with the DFT-optimized structure of the isolated ion (Table 1). The anions are stacked one over the other in a side-by-side arrangement (Figure 2A).

However, $PPh_4[IrCl_5(NO)]$ and $AsPh_4[IrCl_5(NO)]$, both octahedral, have a rather different crystal structure (Figure 2B and Supporting Information). Their crystal lattices have two interesting features: the phenyl rings are perfectly stacked one over the other, determining the lattice structure; and the anions are placed in a perfectly linear arrangement, reminiscent of an infinite "wire." This wire could be considered as a molecular nanowire embedded in a matrix of PPh_4^+ (or $AsPh_4^+$) counterions, leaving the "hole" occupied by the anions. Nanowires are anisotropic nanocrystals with large aspect ratios (length/diameter),[13] while molecular nanowires are wires composed of repeating molecular units, either inorganic or organic.[14] Nevertheless, the peculiar wire-like arrangement and the short NO^+–Cl^- distance between the N–O moiety of one anion and the *trans* chloride of the nearby one above (2.8 Å) observed in the case of $PPh_4[IrCl_5(NO)]$, as compared with its Na^+ and K^+ counter-

Abstract in Spanish: *El nitrosilo presente en el anión $[IrCl_5(NO)]^-$ es probablemente el más electrofílico que se conoce hasta la fecha. Este hecho se refleja claramente en su altísima frecuencia en el espectro infrarrojo del sólido, su comportamiento electroquímico y su sorprendente reactividad en solución. La estructura cristalina del complejo $PPh_4[IrCl_5(NO)]$ presenta una disposición peculiar de los aniones $[IrCl_5(NO)]^-$. Estos se encuentran ubicados de forma lineal, semejando un cable, y manteniendo una distancia corta (2.8 Å) entre el NO de uno de los aniones y el cloro trans del siguiente. Para el mismo anión $[IrCl_5(NO)]^-$ pero con diferente contraión, $Na[IrCl_5(NO)]$, los aniones se ubican uno al lado del otro (lateralmente), y no uno sobre el otro, como en el caso mencionado anteriormente. La distribución electrónica correspondiente al cristal de sodio, se puede describir como un singulete de capa cerrada Ir^{III}–NO^+, situación esperable para un complejo que posee un metal de la tercera serie de transición y d^6. Sin embargo, para el complejo $PPh_4[IrCl_5(NO)]$ se observa una llamativa perturbación electrónica. Probablemente, son las interacciones donor–aceptor $NO^\bullet$–Cl^- a lo largo de un gran número de unidades de $[IrCl_5(NO)]^-$ las que favorecen una distribución electrónica diferente, la de singulete de capa cerrada Ir^{IV}–$NO^\bullet$. Esta conclusión está basada en evidencias experimentales obtenidas por XANES que demuestran que el estado de oxidación formal para el iridio en $PPh_4[IrCl_5(NO)]$ es +4, en comparación con el valor de +3 encontrado para el mismo metal en el complejo $K[IrCl_5(NO)]$. Los resultados de cálculos de DFT de estado sólido concuerdan con lo planteado anteriormente. Se ha encontrado que el estado fundamental para el $[IrCl_5(NO)]^-$ en el cristal de PPh_4^+ está descripto por un singulete de capa abierta con la mitad de la densidad de spin mayoritariamente localizada en un orbital centrado en el metal, y la otra mitad en uno correspondiente al NO. Esta perturbación podría verse como una promoción electrónica desde un orbital mixto metal–cloro hacia otro orbital metal–NO, debido a la pequeña diferencia que existe entre el HOMO–LUMO en el caso de $PPh_4[IrCl_5(NO)]$. Esto puede estar originado por interacciones electrostáticas que resultan de la cercanía y la particular disposición de cable que presentan los centros metalicos de Ir. Se considera que las fuertes interacciones de tipo π–π entre los anillos bencénicos son las responsables de que el anión adopte esta disposición en el cristal. Con respecto a la geometría de la unidad Ir–N–O, los resultados experimentales y teóricos indican que se encuentra parcialmente angular y que el nitrógeno está ligeramente desplazado respecto al eje Cl(trans)–Ir.*

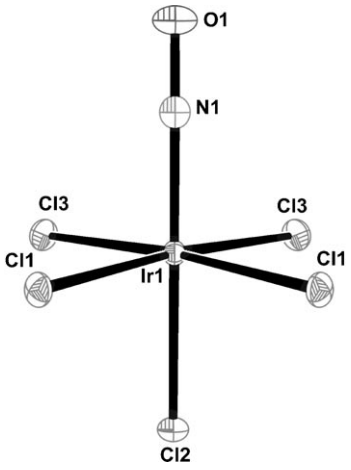

Figure 1. Anion portion of the Na[$IrCl_5$(NO)] X-ray crystal structure. Thermal ellipsoids are drawn at the 50% level.

Table 1. FTIR NO stretching frequencies and selected structural parameters for $[IrCl_5(NO)]^-$ and related species.

Compound	ν_{NO} [cm^{-1}]	∢MNO [°]	d_{N-O} [Å]	d_{M-N} [Å]
K[$IrCl_5$(NO)][a]	2006	174.3	1.124	1.760
Na[$IrCl_5$(NO)][a]	1986	172.9	1.140	1.760
PPh_4[$IrCl_5$(NO)] (tilted)	1952[b]	166.9[c]	1.17[c]	1.77[d]
$[IrCl_5(NO)]^{-}$[e]	1946	179.2	1.158	1.750
	2027	178.9	1.140	1.764
$[IrCl_5(NO)]^{2-}$[e]	1650	139.9	1.190	1.860
	1755	141.1	1.180	1.873
K[$IrBr_5$(NO)][f]	1953	170.3	1.166	1.710
Na_2[$Fe(CN)_5$(NO)][g]	1944	175.7	1.124	1.653
Na_2[$Ru(CN)_5$(NO)][g]	1926	173.9	1.127	1.776

[a] Experimental data from KBr pellet, and X-ray crystallography. [b] Experimental data from KBr pellet. [c] DFT optimization in the solid state (see below). [d] EXAFS data (see below). [e] DFT optimized structure in vacuo, DZPV basis sets for N, O and Cl, LANL2DZ basis sets and pseudopotential for Ir; BPW91 functional for the first line and B3LYP for the second one. [f] Ref. [8]. [g] Ref. [4].

parts, suggested that the electronic distribution for this third-row transition metal complex was unusual. We therefore investigated the possibility of an electronic distribution represented by Ir^{IV}–$NO^{\bullet}$ for the PPh_4^+ complex, instead of Ir^{III}–NO^+ (as for the K^+ and Na^+ ones). In principle, the lone electron on $NO^{\bullet}$ could be paired or unpaired with the metal-based lone electron, forming a singlet or a triplet species respectively. This electronic isomerism could be viewed as produced by packing forces in the crystal, which would be very rare for second- or third-row transition metals. The possibility of a triplet ($Ir^{\uparrow}$–$NO^{\uparrow}$) was discarded because of the diamagnetism of PPh_4[$IrCl_5$(NO)], as observed by EPR and SQUID measurements (Supporting Information). Therefore, the expected situation was a singlet species ($Ir^{\uparrow}$–$NO^{\downarrow}$) with a low-spin Ir^{IV} center ($S=+^1/_2$) coupled antiferromagnetically to $NO^{\bullet}$ ($S=-^1/_2$). In the gas phase, a nitrosyl complex in an open-shell state (triplet or singlet) is less stable than the linear CSS (closed-shell singlet) (Supporting Information). Why, then, would the electronic perturbation

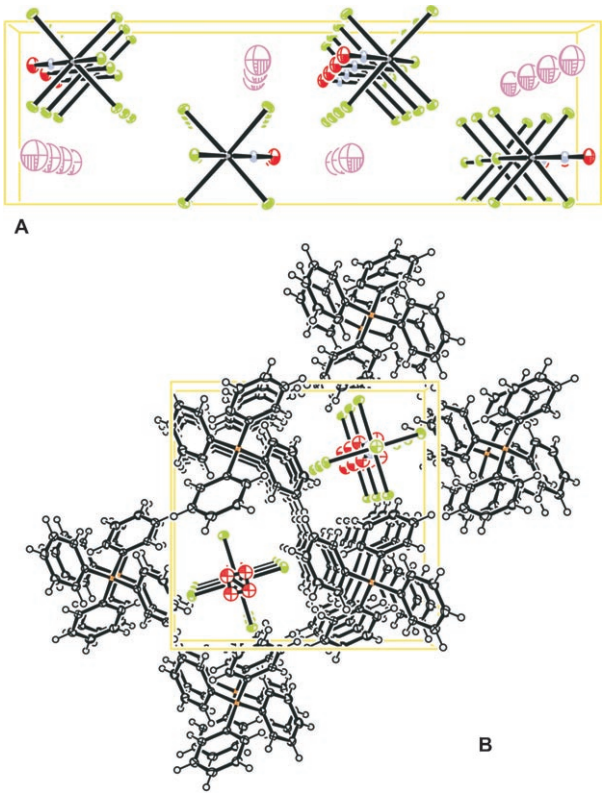

Figure 2. X-ray crystal structures (001 view) of A) Na[$IrCl_5$(NO)] and B) PPh_4[$IrCl_5$(NO)]. Thermal ellipsoids are drawn at the 50% level. Unit cells are shown in yellow, O in red, Cl in green, N in blue, C and H in black, Ir in A) gray or B) black, P in orange, and Na in pink.

occur in the solid state? As mentioned above, π–π stacking interactions among the phenyl rings are very probably taking place, since the Ir–Ir distance between two anions is less than the minimum required for stable linear nitrosyls (see below). In the case of benzene, the π–π stacking energy of interaction could be around 2–4 kcal mol^{-1}.[15,16] Since in the case of the phosphonium complex there are four rings per anion, 8–16 kcal mol^{-1} would be the approximate energy of the π–π stacking interactions, which is in the range of the energy difference between the OSS (open-shell singlet) and the CSS for the isolated anion in vacuo (≈14 kcal mol^{-1}; see Supporting Information).

Strong experimental evidence supporting the Ir^{IV}–$NO^{\bullet}$ configuration in PPh_4[$IrCl_5$(NO)] was provided by X-ray absorption near-edge structure (XANES) measurements in the solid state at the L_3 edge (Figure 3). The L_3 absorption edge of transition metals has important features which can reveal the occupancy of d states. For instance, third-row transition metals exhibit a large peak after the absorption edge, usually called a "white line". The white line intensity is directly related to the density of unoccupied states. In particular, the Ir L_3-edge XANES spectrum is characterized by this white line, which corresponds primarily to the electric dipole allowed electronic transitions from 2p states to 5d ones. For the third-row transition metals it has been shown that the position of the absorption edge and the intensity of the

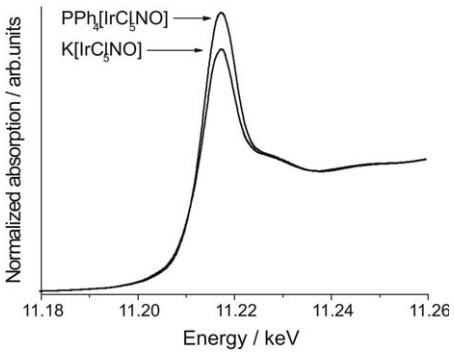

Figure 3. XANES spectra at the Ir L_3 edge.

white line at the L_3 edge are both directly related to the oxidation number of the absorbing atom.[17] The higher the oxidation state of the metal, the more positive the overall charge of the atom; then more energy is required to excite an electron out of an orbital.[18] Besides, as the oxidation number of the absorbing atom increases, the edge moves to higher energy and the intensity of the white line increases because of the higher density of empty states. For both energy shifts and white-line intensity variations, XANES becomes an ideal tool for the determination of changes in the oxidation state of metals.[18,19] Sometimes the variation in the oxidation state results in a smaller energy shift than the intrinsic energy uncertainty at the corresponding electronic level, so this methodology is not sensitive enough to determine the energy shift and the only parameter suitable for determination of the oxidation state is the intensity of the white line. Moreover, when the nature of the moieties surrounding the absorbing atoms differs among samples, the shift is not an unequivocal parameter since the total energy shift comprises an intricate superposition of factors (for example, geometry, orbital hybridization, charge transfer).[20]

Like the L_3 white lines, the L_2 white lines for Ir are attributed to transitions from 2p orbitals to partially occupied bands at the Fermi level with a largely 5d character. Since precisely *d* electrons are involved in Ir–Cl or Ir–N bonds, the L_2- and L_3-edge XANES spectra will be particularly sensitive to changes in redox state. L_2 and L_3 are associated with the dipole allowed electronic transitions $2p_{1/2} \rightarrow 5d_{3/2}$ and $2p_{3/2} \rightarrow 5d_{5/2}$ respectively, but the increment at the L_3 white line does not necessarily imply that L_2 should also increase, because the overlapping differs at the $5d_{5/2}$ and $5d_{3/2}$ levels of Ir in the molecule. Moreover, the constant intensity of the L_2 white line indicates that the increment originates mainly in variations in the occupancy at the $5d_{5/2}$ level. It is interesting that the XANES spectra at the L_2 edge are exactly the same for $PPh_4[IrCl_5(NO)]$ and $K[IrCl_5(NO)]$ (see Supporting Information), demonstrating that the results observed at the L_3 edge do not correspond to experimental artifacts such as thickness effects or inhomogeneities in the sample.[21]

The area of the absorption peak in Figure 3 at around 11.22 keV for $PPh_4[IrCl_5(NO)]$ is notably larger than that for $K[IrCl_5(NO)]$, indicating a higher density of unoccupied states for the Ir center: that is, a higher oxidation state for Ir in $PPh_4[IrCl_5(NO)]$. The expected energy shift is not observable for the two different samples because the resolution of the energy measurements (approximately 5 eV) is not great enough for the small differences expected (ca 1 eV) to be detected.

In the particular case of Ir L edges, the increment in the Ir L_3 white-line intensity with its oxidation state was verified by XANES measurements for three different Ir reference compounds with similar close surroundings but different oxidation states (references: $Ir^{IV}L_6$, $K_2[IrCl_6]$; $Ir^{III}L_6$, $K_3[IrCl_6]$; $Ir^{I}L_2Cl_2$, $Ir_2(C_8H_{12})_2Cl_2$). To compare the two sets of compounds, the white-line area was determined and plotted versus the oxidation state for the references, giving an approximately linear relationship. Under this approximation, from the white-line area of $K[IrCl_5(NO)]$ and $PPh_4[IrCl_5(NO)]$ the oxidation state for the latter was determined as 3.9, that is, 0.9 units higher than for the $K[IrCl_5(NO)]$ sample (see Figure 4).

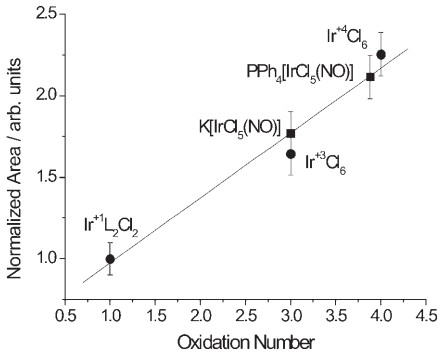

Figure 4. Correlation between Ir L_3 white-line area and Ir oxidation states for both $[IrCl_5(NO)]^-$ samples. ■: linear fit line for the reference compounds; ●: experimental results.

To provide more evidence for the OSS configuration, DFT calculations were performed both in vacuo on the isolated anion $[IrCl_5(NO)]^-$, and in the solid state on the extended, infinitely repeated crystallographic structure of $PPh_4[IrCl_5(NO)]$. In agreement with the XANES results, the total and absolute magnetization in the solid (single-crystal X-ray geometry), computed as $\int(\rho\uparrow-\rho\downarrow)\mathrm{d}r$ and $\int|\rho\uparrow-\rho\downarrow|\,\mathrm{d}r$ respectively, were 0.0 and 4.0 *e*, consistent with an OSS (see Supporting Information). An absolute magnetization of 2.0 *e* is indicative of open-shell systems with two unpaired electrons; in this case a value of 4.0 originates in two metallic centers per unit cell. The same results were obtained for a DFT partially optimized structure in the solid state (see below), although in this case the OSS is 8.7 kcal mol^{-1} more stable than the experimental X-ray crystal structure. Figure 5 displays the total spin density as obtained from the solid-state calculations, showing half of the spin density localized on a metal-centered orbital and slightly spread onto the equatorial chlorides, and the other half localized on an

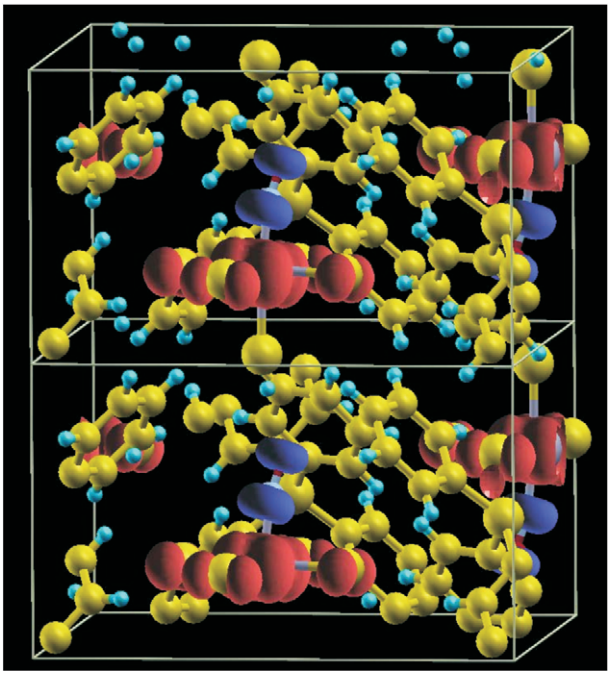

Figure 5. Electronic spin density for the partially optimized structure of $PPh_4[IrCl_5(NO)]$, calculated by DFT in the solid state ($d_{Ir-Ir}=7.8$ Å, as in the crystal structure). The navy blue and red lobes represent unpaired electron densities of opposite spin.

NO-based orbital. For the same compound, the electronic structure of the CSS, with total and absolute magnetization both equal to zero, was also converged, being 13.7 kcal mol^{-1} higher in energy than the OSS. The triplet could not be converged in any case, indicating that it is not a stable electronic state. On the other hand, although DFT calculations do not account for the dispersive forces arising between aromatic rings, we do not expect this flaw to produce any relevant effect on the NO geometry or the spin density, since all atoms involved in π–π stacking were frozen at their experimental coordinates during the calculations.

As an electron transfer or another type of electronic influence could take place from the phosphonium counterions to $[IrCl_5(NO)]^-$, calculations in the solid state were also performed by removing the counterions from the crystal cell, leaving isolated molecular nanowires. In this case also, an OSS was obtained as the ground state (Figure 6), indicating that there are no important electronic effects derived from the presence of the counterions. The likelihood of an electronic transition taking place during the X-ray measurements was also discarded since the IR spectra obtained immediately after irradiation appeared no different from that corresponding to the starting material, and no color changes were observed during or after irradiation.

It is striking that when the Ir centers of the structure in Figure 6 are located 21 Å apart instead of 7.8 Å, the ground state is represented by the CSS. It is evident from the above that the proximity of the anions and their singular "nanowire-like" arrangement are responsible for the stabilization of the OSS, probably because of electrostatic interactions.

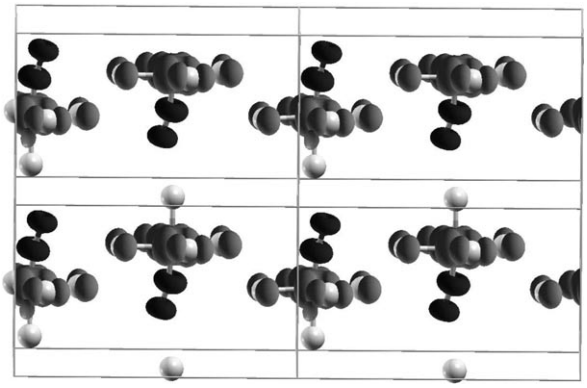

Figure 6. Electronic spin density for the anion portion of the partially optimized structure of $PPh_4[IrCl_5(NO)]$, calculated by DFT in the solid state ($d_{Ir-Ir}=7.8$ Å). The black and dark gray lobes represent unpaired electron densities of opposite spin.

A possible explanation for the open-shell configuration is provided by inspecting the frontier orbitals in $[IrCl_5(NO)]^-$ dimers and trimers. Consistently with this, DFT in-vacuo calculations show that the degeneracy of the orbitals corresponding to the isolated anions is broken for dimers and trimers with Ir–Ir distances constrained to the value observed for the crystal structure (7.807 Å). The energy gap between the HOMO and the LUMO (ΔE_{H-L}) for each of the systems, calculated by DFT in vacuo, decreases considerably for dimers and trimers. For example, in the case of the in-vacuo optimized geometry: $\Delta E_{H-L}=1.31$, 0.70, and 0.40 eV for the monomer, dimer, and trimer, respectively (taking the last two as whole units). For a trimer with $d_{Ir-Ir}=$ 21 and 31 Å, $\Delta E_{H-L}=1.00$ and 1.14 eV, respectively. These results point toward the formation of a conducting band by strong interactions between the anions.

Raman spectra of the two types of crystals provide further support for the results above. For $K[IrCl_5(NO)]$ the NO stretching mode (ν_{NO}) is observed at 1976 cm^{-1} with very low intensity, while in $AsPh_4[IrCl_5(NO)]$ (which behaves analogously to the PPh_4^+ salt and has a crystal structure very similar to that of $PPh_4[IrCl_5(NO)]$), this band gains intensity and shifts down to 1955 cm^{-1} (Figure 7 and Supporting Information). IR spectra show intense bands at $\nu_{NO}=$ 2006 cm^{-1} for $K[IrCl_5(NO)]$ and 1952 cm^{-1} for $AsPh_4$-$[IrCl_5(NO)]$ and $PPh_4[IrCl_5(NO)]$.

Nitrosyl-based reduction, $M-NO^+ \rightarrow M-NO^{\bullet}$, causes a large downshift ($\approx$300 cm^{-1}) of the ν_{NO} band, as well as an increase in the Raman compared with the IR activity.[4,21,22] On the other hand, metal-based oxidation, $M^{III}-NO^+ \rightarrow M^{IV}-NO^+$, shifts the ν_{NO} band in the opposite direction due to diminished backbonding. This shift is expected to be smaller than for nitrosyl reduction, as observed experimentally for different MNO moieties.[4,22,23] Thus, the net effect for an $Ir^{III}-NO^+ \rightarrow Ir^{IV}-NO^{\bullet}$ transition is expected to be a relatively small downshift of the ν_{NO} band, as observed in the present work.

The weak Raman band observed at 556 cm^{-1} for K-$[IrCl_5(NO)]$ is assigned tentatively to Ir-N-O bending (δ_{IrNO})

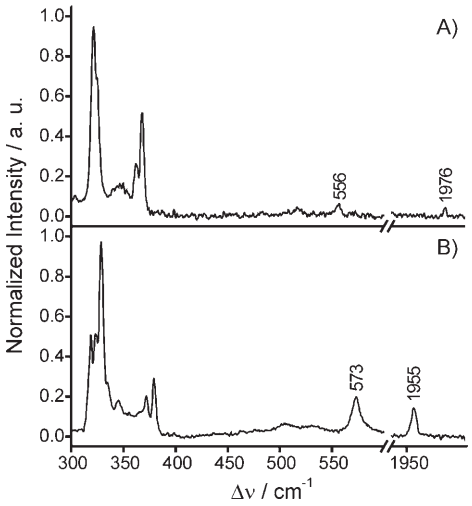

Figure 7. Single-crystal Raman spectra recorded with 514 nm excitation at 83 K. A) $K[IrCl_5(NO)]$; B) $AsPh_4[IrCl_5(NO)]$. The intensities are normalized by the strongest low-frequency band for a better comparison.

although some degree of mixing with ν_{Ir-N} modes cannot be ruled out.[24] For $AsPh_4[IrCl_5(NO)]$ crystals, this band gains intensity and shifts to higher energy, 573 cm^{-1}. Both the increased intensity and the higher frequency are indicative of a tilted Ir^{IV}–$NO^{\bullet}$ moiety in the latter crystals.[25]

Geometry of the Ir–N–O moiety: When DFT in-vacuo calculations were performed for $[IrCl_5(NO)]^-$ dimers and trimers (Figure 8) with Ir–Ir distances constrained to the value observed for the crystal structure (7.807 Å) and the arrangement corresponding to the phosphonium compound, some bending and tilting for Ir-N-O was observed, indicating that packing forces (probably π–π stacking between the phenyl rings) could be operating in the crystal. Similar results were observed when the optimization of one $[IrCl_5(NO)]^-$ unit was performed in a background of NPA-calculated charges (NPA, natural population analysis) corresponding to two $[IrCl_5(NO)]^-$ units and 12 counterions, all of them located as in the X-ray PPh_4^+ structure (see Supporting Information). The interactions mentioned above seem to be producing an

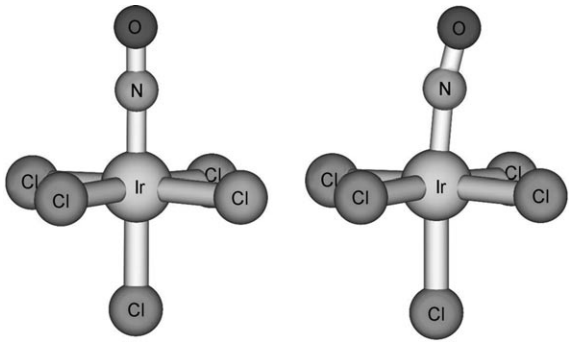

Figure 8. Optimized structure of two $[IrCl_5(NO)]^-$ units with the Ir–Ir distance constrained at the experimental X-ray value in the PPh_4^+ structure.

Ir–Ir distance constraint, which becomes too short to accommodate anions with a linear Ir-N-O moiety. In the similar case of $(AsPh_4)_2[Fe(CN)_5NO]$, where again the cations determine the lattice structure and leave little space for the anions,[25,26] the anions' preferred position is in a tilted orientation instead of just the M–N–O moiety being bent or tilted. Therefore, in the case of $PPh_4[IrCl_5(NO)]$, an interaction between the *trans* chloride of one anion and the NO of the anion below it could be taking place, helping to form the "wire" mentioned above (the Cl–O distance is 2.8 Å).

Although the X-ray measurements in the case of $PPh_4[IrCl_5(NO)]$ were of excellent quality and the structure was perfectly defined for the counterions and all the Ir–Cl bonds, due to crystal disorder some uncertainty remained regarding the structure of the Ir-N-O moiety. Refinements were performed with anisotropic or isotropic parameters (see Supporting Information; an almost equal structure was obtained for $AsPh_4[IrCl_5(NO)]$). In all cases a large ellipsoid was observed surrounding the N atom, suggesting that it is probably located slightly off-axis. However, crystal disorder—which gives rise to four different N atom orientations—and the presence nearby of the heavy Ir atom prevent establishment of the exact position of the N atom. The distance between its four different orientations are close to the resolution of the instrumental. While under the experimental conditions of our measurements the maximum achievable instrumental resolution is approximately 0.4 Å, the distance between the N atom positions according to the DFT optimizations in the solid state (see below) would be 0.43 Å.

DFT solid-state calculations were performed on the crystal structure in periodic boundary conditions, relaxing the spatial coordinates of the N and O atoms while freezing the rest of the coordinates at the experimental X-ray positions. The use of DFT to complement X-ray results when structural disorders blur the crystallographic parameters is now a common practice, often applied to elucidate the bonding mode of diatomic ligands such as NO or CO in different transition metal complexes (see, for example, refs. [27] and [28]). The optimized Ir–N and N–O distances are consistent with the X-ray data, with the N–O moiety exhibiting a 7° tilt and a concomitant increase in the Ir-N-O angle. A visual comparison with the single-crystal X-ray geometry shows that the N and O atoms of the optimized structure are within the boundaries of the thermal ellipsoids corresponding to the X-ray refinement (Figure 9).

To determine the Ir near-neighbor environment, X-ray absorption fine structure (EXAFS) measurements were performed for $K[IrCl_5NO]$ and $PPh_4[IrCl_5(NO)]$ (Figure 10 and Supporting Information). EXAFS spectroscopy refers to the oscillatory structure in the X-ray absorption coefficient beyond a 50 eV threshold. The fit of this oscillation gives information about the surroundings of the absorbing atom. In particular, the type, number, and bond lengths of the atoms around the absorbing atom can be obtained. EXAFS analysis is not limited to first neighbors, and distance determinations are now often comparable in accuracy with those from

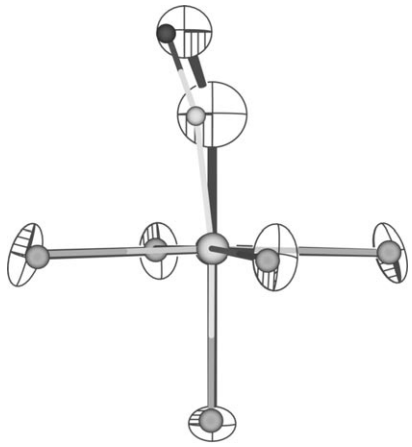

Figure 9. In the background, DFT (solid-state) geometry of the anion portion of $PPh_4[IrCl_5(NO)]$ superimposed on the thermal ellipsoids corresponding to the structure determined by single-crystal X-ray diffractometry (in the foreground; only one of the four equivalent O atom positions is shown).

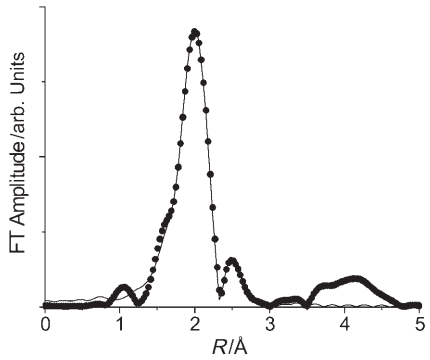

Figure 10. Fourier transform amplitude of the EXAFS spectrum for $PPh_4[IrCl_5(NO)]$ (dots) and the obtained fit (full line) considering the DFT (solid-state) optimization as data input for the simulation.

X-ray diffraction measurements.[29] In addition, a multiple scattering analysis of the EXAFS spectrum can determine atom configuration where three atoms are aligned or almost aligned,[30] because of the shadowing or focusing effect.[31]

Simulations for different geometries for $PPh_4[IrCl_5(NO)]$ were made using the FEFF6 code.[32] The small peak at about 2.5 Å in Figure 10 is due to both simple scattering from oxygen atoms and multiple scattering paths for Ir-N-O and could be reproduced only by the simulation of structural arrangements where these three atoms were almost aligned. These conditions were met for an Ir-N-O angle greater than approximately 160°. Therefore, a poor fit was obtained when the X-ray crystal structure was used as data input (the Ir-N-O angle in this case is 149°). However, the geometry corresponding to the DFT optimization in the solid state previously described (see Supporting Information, and Figures 5 and 6) gave an excellent fit.

Compared with other $\{MNO\}^6$ complexes with similar structural characteristics (Table 1), specifically N–O distances and M-N-O angles, the IR stretching frequency for NO in $PPh_4[IrCl_5(NO)]$ falls in the same frequency region, around 1950 cm^{-1}. As expected when an "extra" electron is located in an NO antibonding orbital, the N−O distance is augmented, and its value is between the N−O distances for $K[IrCl_5(NO)]$ or $Na[IrCl_5(NO)]$ and that calculated for $[IrCl_5(NO)]^{2-}$ (Table 1). The correlation of the N−O distance with ν_{NO} is excellent (Supporting Information). Moreover, a normal-mode analysis shows that d_{NO} should be around 1.17 Å for the observed ν_{NO} stretching frequency.

In summary, we consider that the DFT optimization in the solid state provides the more accurate structural parameter set for the Ir-N-O moiety, while EXAFS provides excellent parameters for d_{Ir-N}, d_{Ir-O}, $d_{Ir-Cl(trans)}$ and $d_{Ir-Cl(eq)}$. These last two distances and d_{Ir-Ir} are also provided accurately by the X-ray determination. A selected set of parameters, which gives a reasonably accurate geometry for the Ir-N-O moiety of $PPh_4[IrCl_5(NO)]$, is that shown in Table 1. However, regardless of the exact value for the Ir-N-O angle and the N−O distance, it is clear that the nitrosyl shows a partially bent/tilted conformation and that a linear N−O does not fit due to the constraint imposed by the short Ir−Ir distance in the "wire-like" arrangement. This peculiar arrangement is probably responsible for the electronic perturbation.

Conclusion

The distribution of electrons in Ir^{III}–NO^+ versus Ir^{IV}–$NO^{\cdot}$ in the case of $[IrCl_5(NO)]^-$ can be viewed as an electron promotion from a metal–chloride to a metal–NO orbital due to a decrease in the HOMO–LUMO gap of $PPh_4[IrCl_5(NO)]$ in the solid state. This is induced by electrostatic interactions acting as a result of the closeness and "wire-like" spatial distribution of the Ir metal centers. This singular arrangement is imposed by lattice forces produced by π–π stacking interactions between the phenyl rings in PPh_4^+.

Our theoretical and experimental evidence suggests that this is an interesting case of electronic perturbation in a third-row transition metal complex in the ground state giving rise to valence tautomerism. The high sensitivity of the M-N-O moiety toward the environment, its high electrophilicity, and its interaction with the nearby chloride ligand in this singular "wire-like" $[IrCl_5(NO)]^-$ arrangement seems to be the motive force for the unique structural end electronic behavior of pentachloronitrosyliridate, going beyond the original $\{MNO\}^6$ formalism proposed by Enemark and Feltham and which predicts that isolated $\{IrNO\}^6$ units should be linear.

Experimental Section

General procedures: All experimental manipulations were performed under anaerobic and anhydrous conditions using standard Schlenk procedures and a dry box. $K[IrCl_5(NO)]$ was purchased from Strem and purified by recrystallization from CH_3CN. $Na[IrCl_5(NO)]$ was prepared by addition of a 10-fold excess of NaCl to a HCl (1 M) solution of the potassium salt. The solution volume was reduced in a rotary evaporator and

the supernatant kept in a refrigerator for three days. One HCl molecule per $Na[IrCl_5(NO)]$ unit was observed in the X-ray crystal structure. Tetraphenylphosphonium pentachloronitrosyliridate, $PPh_4[IrCl_5(NO)]$, was obtained by slowly adding a concentrated solution of tetraphenylphosphonium bromide (0.50 M in CH_3CN) to a solution of $K[IrCl_5(NO)]$ (0.09 M in CH_3CN) and washing the precipitate three times with deionized distilled water. The dry, light brown crystals were dissolved in warm CH_3CN (60 °C) and this solution was allowed to reach room temperature very slowly. The resulting crystals were suitable for X-ray analysis. An identical technique was employed to obtain the tetraphenylarsonium analogue.

Instrumental procedures: UV/Vis spectra were recorded using a Hewlett Packard 8453 diode array spectrometer with quartz cuvettes (10 mm optical path).

IR spectra were recorded using a Nicolet Avatar 320 FTIR spectrometer with either KBr pellets or a Spectra Tech cell for liquids with CaF_2 ($\varnothing =$ 3 cm) windows and a 0.1 mm Teflon spacer.

Cyclic voltammetry in aqueous solvents was carried out at a 100 $mV\,s^{-1}$ scan rate using a three-electrode configuration (glassy carbon working electrode, Pt counter-electrode, Ag/AgCl reference) and a TeQ-03 potentiostat and function generator.

For resonance Raman measurements, crystals were placed in a cooling/heating microscope stage (Linkam THMS 600) to vary the temperature between −190 and 200 °C with a precision of ±0.1 °C. Raman spectra were recorded in backscattering configuration using a confocal microscope attached to a single-stage spectrograph (XY-Jobin Yvon) equipped with a 1800 lines mm^{-1} grating and liquid nitrogen cooled, back-illuminated CCD detector. The spectral resolution was approximately 2 cm^{-1} and the increment per data point was 0.47 cm^{-1}. Elastic scattering was removed with a super Notch filter (Kaiser). Measurements were performed under nonresonant conditions using the 514.5 nm line of an argon ion laser (Innova 70C; Coherent). To avoid laser-induced damage of the crystal, laser power at the sample was kept below 600 μW and accumulation times were 10–30 s. The values reported for each temperature are the averages of at least three independent measurements on different crystals. Before and after each measurement, crystals were imaged to confirm that they were not damaged. For laser powers above 5 mW, damage becomes evident as a dark spot (see Supporting Information).

For EXAFS and XANES measurements, X-ray absorption spectra were measured in the D04B-XAS beamline at the National Synchrotron Light Laboratory (LNLS), Campinas, Brazil. EXAFS and XANES spectra at the Ir L_3 (11215 eV) edge were acquired in transmission mode at ambient conditions using a Si(111) crystal monochromator in the 11100–12300 eV energy range. Three ion chambers were used as detectors. The sample was positioned between the first and second detectors and an Ir foil was placed between the second and third ones. In order to obtain a better signal-to-noise ratio, two or three spectra were averaged. The raw data were processed using the Athena program.[33] The AUTOBK algorithm was used to fit a smoothly varying background function to the data and to extract the EXAFS oscillation. The Arthemis program[33] was used for the analysis of these data. Theoretical standards were computed using the FEFF6 code[31] and used in the analysis. The XANES normalization was performed with Athena[33] by matching to the Cromer–Liberman calculations for the absorption of a free atom[33,34] at energies far below and above the edge.

The magnetic susceptibilities of solid complexes were measured in the temperature range 1.5–300 K with a SQUID susceptometer (MPMS Quantum Design Inc.) with an external field of 1.0 T. Multiple-field variable-temperature measurements were made at three different fields for which the magnetization was equidistantly sampled on a T^{-1} temperature scale. The experimental data were corrected for underlying diamagnetism by application of tabulated Pascal's constants.

The EPR spectra were recorded at (25 ± 1) °C and 9.8 GHz (X band) in an ER-200 spectrometer (Bruker Analytische Messtechnik GmbH, Karlsruhe, Germany). The samples were placed in glass capillaries (1 mm i.d.), sealed at both ends, and housed in 4 mm quartz tubes containing silicone oil to maintain temperature uniformity. The field modulation frequency was 100 KHz, and its amplitude was well below 30 % of the minor linewidths in each case, to avoid spectral shape distortions.

For the X-ray diffraction studies, data were collected in a Nonius Kappa CCD diffractometer, $Mo_{K\alpha}$ radiation ($\lambda = 0.71073$ Å), with a graphite monochromator, $T = 120(2)$ K. The data were processed with Denzo Scalepack and the refined structure was solved by the Patterson method with SHELXS with full-matrix least-squares refinement based on F^2 with SHELXL-97. H atoms were treated by a mixture of independent and constrained refinement. Further details of the crystal structure investigations may be obtained from the Fachinformationszentrum Karlsruhe, 76344 Eggenstein-Leopoldshafen, Germany (fax: (+49)7247-808-666; e-mail: crysdata@fiz-karlsruhe.de) on quoting the depository numbers CSD-416353 ($Na[IrCl_5(NO)]\cdot HCl$), CSD-417400 ($PPh_4[IrCl_5(NO)]$), and CSD-417399 ($AsPh_4[IrCl_5(NO)]$).

Crystal and collection data and refinement for $Na[IrCl_5(NO)]\cdot HCl$: H atoms are not included in the X-ray refinement. Cl_6IrNO, $M_r = 457.90$, prisms, crystal size $0.25\times0.10\times0.10$ mm^3, orthorhombic, space group: *Pnma*, $\theta = 2.55$–$27.48°$, $a = 22.366(5)$, $b = 6.8800(14)$, $c = 5.9910(12)$ Å, $F(000) = 820$, $V = 921.9(3)$ $Å^3$, $Z = 4$, $\rho_{calcd} = 3.299$ $g\,cm^{-3}$, $\mu = 16.200$ mm^{-1}, $2\theta_{max} = 54.92°$, limiting indices $0 \le h \le 28$, $0 \le k \le 8$, $0 \le l \le 7$, measured/independent reflections = 1132/1132, 1005 reflections with $> 2\sigma(I)$, $R_{int} = 0.0450$. Refinement based on F^2, number of reflections/parameters = 1132/55, $R = 0.0333$ (based on $F^2 > 2\sigma F^2$)), $\omega R(F^2) = 0.0991$, $S = 1.116$, $(\Delta/\sigma)_{max} = 0.011$, $\Delta\rho_{max} = 2.081$ e $Å^{-3}$, $\Delta\rho_{min} = -1.734$ e $Å^{-3}$.

Crystal and collection data and refinement for $PPh_4[IrCl_5(NO)]$: $C_{24}H_{20}Cl_5IrNOP$, $M_r = 738.83$, orange prisms, crystal size $0.1\times0.05\times0.05$ mm^3, tetragonal, space group: *P4/n*, $\theta = 2.55$–$27.48°$, $a = b = 12.8270(2)$, $c = 7.8070(2)$ Å, $F(000) = 712$, $V = 1284.50(4)$ $Å^3$, $Z = 2$, $\rho_{calcd} = 1.910$ $g\,cm^{-3}$, $\mu = 5.798$ mm^{-1}, $2\theta_{max} = 54.94°$, limiting indices $-16 \le h \le 16$, $-11 \le k \le 11$, $-8 \le l \le 10$, measured/independent reflections = 2737/1484, 1449 reflections with $> 2\sigma(I)$, $R_{int} = 0.0253$. Refinement based on F^2, number of reflections/parameters = 1484/78, $R = 0.0327$ (based on $F^2 > 2\sigma F^2$)), $\omega R(F^2) = 0.0869$, $S = 1.083$, $(\Delta/\sigma)_{max} = 0.004$, $\Delta\rho_{max} = 2.507$ e $Å^{-3}$, $\Delta\rho_{min} = -2.141$ e $Å^{-3}$.

Crystal and collection data and refinement for $AsPh_4[IrCl_5(NO)]$: $C_{24}H_{20}AsCl_5IrNO$, $M_r = 782.78$, orange prisms, crystal size $0.5\times0.5\times0.2$ mm^3, tetragonal, space group *P4/n*, $\theta = 2.55$–$27.48°$, $a = b = 12.8240(18)$, $c = 7.8830(16)$ Å, $F(000) = 748$, $V = 1296.4(4)$ $Å^3$, $Z = 2$, $\rho_{calcd} = 2.005$ $g\,cm^{-3}$, $\mu = 6.950$ mm^{-1}, $2\theta_{max} = 54.92°$, limiting indices $-11 \le h \le 11$, $0 \le k \le 16$, $0 \le l \le 10$, measured/independent reflections = 1487/1487, 1392 reflections with $> 2\sigma(I)$, $R_{int} = 0.0370$. Refinement based on F^2, number of reflections/parameters = 1487/79, $R = 0.0232$ (based on $F^2 > 2\sigma(F^2)$), $\omega R(F^2) = 0.0515$, $S = 1.045$, $(\Delta/\sigma)_{max} = 0.000$, $\Delta\rho_{max} = 1.191$ e $Å^{-3}$, $\Delta\rho_{min} = -1.035$ e $Å^{-3}$.

Computational methodology: All gas-phase DFT calculations were performed by using the Gaussian 98 software package[34,35] and B3LYP[36,37] and/or BPW91[38] functionals with a double zeta plus polarization (DZPV) basis set[39] for N, O, and Cl atoms, and the LANL2DZ basis set and effective core potential for the iridium.[40,41] Calculated structures and other calculated data were obtained by full optimization or by single-point calculation of the X-ray structures (Na^+ salt and PPh_4^+ salt with the anisotropic refinement). In all cases the stability of the wavefunction obtained from DFT calculations was tested and verified and all the integrations were performed using the Gaussian 98 tight criteria. Atomic charges have been calculated using the Mulliken and NPA[42] schemes. The background charge distribution included in the calculations was performed as described under Results and Discussion.[43,44] Open-shell singlet calculations were performed under the broken symmetry formalism. A normal modes analysis was performed in order to obtain vibrational frequencies, force constants, and zero-point energy corrections for the total energy.

Solid-state calculations were performed by using the Quantum ESPRESSO package,[45] featuring periodic boundary conditions, plane-wave basis sets, and pseudopotentials to describe the ion–electron interactions. In the present simulations, Vanderbilt ultrasoft pseudopotentials were used,[46] in combination with plane-wave kinetic energy cutoffs of 20 and 160 Ry to expand the Kohn–Sham orbitals and the charge density, respectively. For the iridium atom, a pseudopotential including nonlinear core

corrections was adopted, with s and d valence electrons. All calculations were spin-polarized, based on the PBE (Perdew, Burke, and Ernzerhof) exchange-correlation functional[47] and gamma-point sampling. The experimental tetragonal unit cell was used, with lattice parameters $a=b=$ 12.827 and $c=7.087$ Å.

Acknowledgements

We are grateful to Carlos Brondino (UNL) for EPR measurements and Eckhard Bill for SQUID measurements. We thank UBA, Fundación Antorchas, CONICET, ANPCyT and LNLS Synchrotron (Proposal XAFS 4642/05), Campinas, SP, Brazil for financial support.

[1] J. S. Stamler, D. J. Singel, J. Loscalzo, *Science* **1992**, *258*, 1898–1902.
[2] KBr pellet: 2006 cm^{-1}; CH_3CN solution: 1953 cm^{-1}.
[3] $E_{1/2}=+$ 0.96 V versus Ag/AgCl in 1 M $HClO_4$; $E_{1/2}=-0.33$ V versus ferrocene in butyronitrile.
[4] M. Sieger, B. Sarkar, S. Záliš, J. Fiedler, N. Escola, F. Doctorovich, J. A. Olabe, W. Kaim, *Dalton Trans.* **2004**, *12*, 1797–1800.
[5] F. Doctorovich, F. Di Salvo, N. Escola, C. Trápani, L. Shimon, *Organometallics* **2005**, *24*, 4707–4709.
[6] L. L. Perissinotti, D. A. Estrin, G. Leitus, F. Doctorovich, *J. Am. Chem. Soc.* **2006**, *128*, 2512–2513.
[7] J. H. Enemark, R. D. Feltham, *Coord. Chem. Rev.* **1974**, *13*, 339–406. In the Enemark–Felthan notation a mononitrosyl complex is described as $\{MNO\}^n$, were n is the total number of electrons in the metal d and NO π* orbitals.
[8] F. J. Bottomley, *J. Chem. Soc. Dalton Trans.* **1975**, *23*, 2538–2541.
[9] R. D. Feltham, J. H. Enemark, *Topics in Inorganic and Organometallic Stereochemistry* (Ed.: G. L. Geoffrey), Wiley, New York, **1981**.
[10] E. Evangelio, D. Ruiz-Molina, *Eur. J. Inorg. Chem.* **2005**, 2957–2971.
[11] A. Caneschi, A. Dei, *Angew. Chem. Int. Ed.* **1998**, *37*, 3005–3007.
[12] PPh_4^+: tetraphenylphosphonium; $AsPh_4^+$: tetraphenylarsonium.
[13] P. Yang, K. Poeppelmeier, *Inorg. Chem.* **2006**, *45*, 7509–7510.
[14] For example, see S. Wang, J-L. Zuo, S. Gao, Y. Song, H-C. Zhou, Y-Z. Zhang, Y-Z. You, *J. Am. Chem. Soc.* **2004**, *126*, 8900–8901.
[15] P. K. C. Paul, *Cryst. Eng.* **2002**, *5*, 3–8.
[16] X. Ye, Z-H. Li, W. Wang, K. Fan, W. Xu, Z. Hua, *Chem. Phys. Lett.* **2004**, *397*, 56–61.
[17] a) W. Schieber, H. Vinek, A. Jentys, *Catal. Lett.* **2001**, *73*, 67–72; b) J. H. Choy, D. K. Kim, G. Demazeau, D. Y. Jung, *J. Phys. Chem.* **1994**, *98*, 6258–6262; c) J. H. Choy, D. K. Kim, S. H. Hwang, G. Demazeau, D. Y. Jung, *J. Am. Chem. Soc.* **1995**, *117*, 8557–8566; d) T. Pauporté, D. Aberdam, J. L. Hazemann, R. Faure, R. Durand, *J. Electroanal. Chem.* **1999**, *465*, 88–95.
[18] a) R. G. Shulman, Y. Yafet, P. Eisenberger, W. E. Blumberg, *Proc. Natl. Acad. Sci. USA* **1976**, *73*, 1384–1388; b) J. M. Ramallo-López, E. J. Lede, F. G. Requejo, J. A. Rodriguez, J-Y. Kim, R. Rosas-Salas, J. M. Domínguez, *J. Phys. Chem. B* **2004**, *108*, 20005–20010.
[19] H. Yoshida, S. Nonoyama, Y. Yazawa, T. Hattori. *Phys. Scripta* **2005**, *T115*, 813–815.
[20] a) J. L. DuBois, P. Mukherjee, T. D. P. Stack, B. Hedman, E. I. Solomon, K. O. Hodgson, *J. Am. Chem. Soc.* **2000**, *122*, 5775–5787; b) T. E. Westre, P. Kennepohl, J. G. DeWitt, B. Hedman, K. O. Hodgson, E. I. Solomon, *J. Am. Chem. Soc.* **1997**, *119*, 6297–6314.
[21] a) E. A. Stern, K. Kim, *Phys. Rev. B* **1981**, *23*, 3781–3787; b) F. W. Lytle, G. van der Laan, R. B. Greegor, E. M. Larson, C. E. Violet, J. Wong, *Phys. Rev. B* **1990**, *41*, 8955–8963.
[22] P. Singh, B. Sarkar, M. Sieger, M. Niemeyer, J. Fiedler, S. Záliš, W. Kaim, *Inorg. Chem.* **2006**, *45*, 4602–4609.
[23] L. Andrews, A. Citra, *Chem. Rev.* **2002**, *102*, 885–911.
[24] B. Benko, N. T. Yu, *Proc. Natl. Acad. Sci. USA* **1983**, *80*, 7042–7046.
[25] S. Hu, J. R. Kincaid, *J. Am. Chem. Soc.* **1991**, *113*, 2843–2850.
[26] E. E. Castellano, O. E. Piro, B. E. Rivero, *Acta Crystallogr. B.* **1977**, *33*, 1728–1732.
[27] R. Garcia Serres, C. A. Grapperhaus, E. Bothe, E. Bill, T. Weyhermüller, F. Neese, K. Wieghardt, *J. Am. Chem. Soc.* **2004**, *126*, 5138–5153.
[28] T. G. Spiro, P. M. Kozlowski, *Acc. Chem. Res.* **2001**, *34*, 137–144.
[29] J. J. Rehr, A. Ankudinov, S. I. Zabinsky, *Catal. Today* **1998**, *39*, 263–269.
[30] B. K. Teo, *J. Am. Chem. Soc.* **1981**, *103*, 3990–4001.
[31] E. Stern, Theory of EXAFS, in *X-ray Absorption Principles, Applications, Techniques of EXAFS, SEXAFS and XANES* (Eds.: D. C. Konisberger and R. Prins), John Wiley and Sons, New York, **1988**, pp.34–36.
[32] S. I. Zabinski, J. J. Rehr, A. Ankudinov, R. C. Albers, M. J. Eller, *Phys. Rev. B* **1995**, *52*, 2995–3009.
[33] B. Ravel, M. Newville, *J. Synchrotron Radiat.* **2005**, *12*, 537–541.
[34] D. T. Cromer, D. Liberman, *J. Chem. Phys.* **1970**, *53*, 1891–1898.
[35] M. J. Frisch, G. W. Trucks, H. B. Schlegel, G. E. Scuseria, M. A. Robb, J. R. Cheeseman, V. G. Zakrzewski, J. A. Montgomery, Jr., R. E. Stratmann, J. C. Burant, S. Dapprich, J. M. Millam, A. D. Daniels, K. N. Kudin, M. C. Strain, O. Farkas, J. Tomasi, V. Barone, M. Cossi, R. Cammi, B. Mennucci, C. Pomelli, C. Adamo, S. Clifford, J. Ochterski, G. A. Petersson, P. Y. Ayala, Q. Cui, K. Morokuma, D. K. Malick, A. D. Rabuck, K. Raghavachari, J. B. Foresman, J. Cioslowski, J. V. Ortiz, A. G. Baboul, B. B. Stefanov, G. Liu, A. Liashenko, P. Piskorz, I. Komaromi, R. Gomperts, R. L. Martin, D. J. Fox, T. Keith, M. A. Al-Laham, C. Y. Peng, A. Nanayakkara, C. Gonzalez, M. Challacombe, P. M. W. Gill, B. Johnson, W. Chen, M. W. Wong, J. L. Andres, C. Gonzalez, M. Head-Gordon, E. S. Replogle, and J. A. Pople, Gaussian 98, Revision A.7, Gaussian Inc., Pittsburgh, PA, **1998**.
[36] A. D. Becke, *J. Chem. Phys.* **1993**, *98*, 5648–5652.
[37] C. Lee, W. Yang, R. Parr, *Phys. Rev. B* **1998**, *37*, 785–789.
[38] A. D. Becke, *Phys. Rev. A* **1988**, *38*, 3098–3100.
[39] N. Godbout, D. R. Salahub, J. Andzelm, E. Wimmer, *Can. J. Chem.* **1992**, *70*, 560–571.
[40] P. J. Hay, W. R. Wadt, *J. Chem. Phys.* **1985**, *82*, 270–283.
[41] W. R. Wadt, *J. Chem. Phys.* **1985**, *82*, 299–310.
[42] A. E. Reed, L. A. Curtis, F. Weinhold, *Chem. Rev.* **1988**, *88*, 899–926.
[43] G. G. Hall, C. M. Smith, *Int. J. Quantum Chem.* **1984**, *25*, 881–890.
[44] C. M. Smith, G. G. Hall, *Theor. Chim. Acta.* **1986**, *69*, 63–69.
[45] S. Baroni, A. Dal Corso, S. de Gironcoli, P. Giannozzi, C. Cavazzoni, G. Ballabio, S. Scandolo, G. Chiarotti, P. Focher, A. Pasquarello, K. Laasonen, A. Trave, R. Car, N. Marzari, A. Kokalj, Quantum ESPRESSO, http://www.quantum-espresso.org/.
[46] D. Vanderbilt, *Phys. Rev. B* **1990**, *41*, 7892–7895.
[47] J. P. Perdew, K. Burke, M. Ernzerhof, *Phys. Rev. Lett.* **1996**, *77*, 3865–3868.

Received: December 7, 2006
Revised: May 12, 2007
Published online: July 18, 2007

